Nanoengineered Thin-film TiO$_2$/h-MoO$_3$ Photocatalysts Capable to Accumulate Photoinduced Charge

T.V. Sviridova[a], L. Yu. Sadovskaya[a], E.M. Shchukina[b], A.S. Logvinovich[a],
D.G. Shchukin[b1], D. V. Sviridov[a]

[a] *Department of Chemistry, Belarusian State University, Minsk, Belarus*
[b] *Stephenson Institute for Renewable Energy, University of Liverpool, UK*

The mosaic films made of TiO$_2$ and hexagonal MoO$_3$ nanoparticles not only demonstrate high activity in the reactions of photooxidation of the adsorbed organics in air conditions but also store the photoinduced charge as the result of MoO$_3$ reduction by photoelectrons injected from titania which behaves as a photogenerating component. The charge accumulated *via* this light-driven reduction is spent under dark conditions in the reaction of molecular oxygen reduction yielding peroxide species. As the result, TiO$_2$/h-MoO$_3$ nanocomposite films retain oxidation ability for *ca*. 4 hours after UV illumination. This photocatalytic material opens fresh avenues in fabrication of self-sterilizing coatings capable to generate reactive oxygen species not only under actinic illumination but also under dark conditions.

Key words: photocatalyst, energy storage, hexagonal MoO$_3$

---

[1] Corresponding author (E-mail: D.Shchukin@liverpool.ac.uk)

1. Introduction

The oxidation and reduction driven by photoholes and excited electrons generated at the UV-irradiated TiO_2 surface make it an effective photocatalytic material for realization of various useful functions, such as removal of toxic compounds and self-sterilization [1-4]. These functions are based on oxidation abilities of reactive oxygen species (ROS) produced *via* photocatalytic reactions (hydroxyl radicals generated by photoholes from TiO_2 valence band reacting with surface adsorbed water and superoxide ions formed due to interaction of photoelectrons from conduction band with molecular oxygen [5,6]). Being strong oxidants, ROS can participate in the series of oxidation reactions [3,7] leading in the destruction of organic contaminants [2,3,8] and are able to cause various damages to microorganisms ensuring their rapid inactivation [9-11].

The intrinsic limitation that comes from basic mechanisms of TiO_2 photocatalysis consists in the fact that oxidation activity of TiO_2 does not retain after illumination is terminated. To overcome this fundamental limitation, several TiO_2-based photocatalytic systems with reductive an oxidative energy storage abilities have been proposed [12-18]. In these hybrid photocatalysts for storage the reductive energy the combinations of titania with tungsten [12-15] and molybdenum [16] oxides as well as with polyoxometallates [17] were used, while for storage the oxidative energy TiO_2 was successfully combined with $Ni(OH)_2$[18].

Despite many studies investigating the charge storage photocatalytic systems, many problems concerning their behavior still remain to be solved and the most important one among them is a lack of effective control over the discharge behavior to ensure the long-term oxidation and pathophysiological activity of pre-illuminated photocatalytic coatings. Here we demonstrate that the careful engineering of hybrid photocatalysts comprising nanocrystalline TiO_2 and fine crystals of hexagonal MoO_3 (*h*-MoO_3) ensures the retaining of oxidation activity of the photocatalyst surface for a

long time after illumination and the radical enhancement of photocatalytic activity under actinic illumination.

2. Experimental

All materials used in the work were purchased from Sigma–Aldrich Chemical Co. and used as supplied. For preparation of solutions the Milli-Q water was used.

The thin-film photocatalysts were prepared using aqueous dispersions of TiO_2 and MoO_3. The aqueous sol of titania was prepared by adding 12.5% NH_4OH dropwise to 2.5 M $TiCl_4$ + 0.65 M HCl aqueous solution cooled to 0 °C under vigorous stirring until pH 5 was reached. The obtained precipitate was then washed with distilled water and dispersed by ultrasonic treatment. The resultant transparent sol was stable for several days even in the absence of stabilizing agents. The size of thus obtained TiO_2 particles (anatase) was of *ca*. 4 nm.

The MoO_3 particles of different morphology were synthesized *via* thermally-induced polycondensation of molybdic acid in aqueous medium. The detailed mechanism behind polycondensation synthesis employing oxoacids is discussed elsewhere [19].

The molybdic acid solution used as a starting material was prepared by acidification of sodium molybdate on a resin. Four synthetic protocols were used to obtain different MoO_3 nano- and microcrystals:

(i) treatment of 0.5 M molybdic acid solution at 100 °C for 4 h (the reaction volume was maintained constant) that yields regular prism-like MoO_3 microcrystals with the average size of 3 μm × 10 μm;

(ii) hydrothermal treatment of 0.2 M molybdic acid in the 75-ml reactor at 200 °C for 4 h yielding needle-like microcrystals with the average length of 15 μm;

(iii) treatment of 0.5 M molybdic acid at 100 °C for 4 min followed by dilution 1:5 to stop nucleation in the solution and incubation of the resultant oxide particles at 100 °C for 4 h to ensure their recrystallization yielding spherical nanoparticles 100-200 nm in size;

(iv)   treatment of 0.5 M molybdic acid at 100 °C for 10 min followed by dilution 1:5 and incubation of the resultant particles at 100 °C for 4 h under conditions far from supersaturation to ensure the dispersing of MoO_3 prisms that yields regular nanocrystals also with a prismatic shape (nanoprisms) with the average size of 80 nm × 300 nm.

Thin-film photocatalysts were prepared by spraying mixtures of TiO_2 sol and MoO_3 suspension onto the glazed ceramic tiles heated to 200 °C. The resultant coatings were then annealed at 450 °C for 1.5 h in air. The MoO_3 loading in the composite was evaluated from Ti:Mo atomic ratio obtained from Rutherford backscattering spectra.   Before the photocatalyst deposition, the surface of the substrate was coated with a silicon dioxide intermediate layer by spraying the SiO_2 sol to prevent migration of sodium ions from a glaze during annealing (the latter factor could adversary affect the photoactivity of titania [20]). According to the AFM measurements thus obtained photocatalytic coatings have a thickness of *ca.* 0.4 μm.

To probe the photocatalytic activity of TiO_2 and $TiO_2:MoO_3$ composite films the reaction of the photodegradation of Rhodamine 6G (*o*-[6-(ethylamino)-3-(ethylimino)-2,7-dimethyl-3*H*-xanthen-9-yl] benzoic acid ethyl ester monohydrochloride) was used. For each measurement a drop (0.1 ml) of 4×10^{-4} M aqueous solution of Rhodamine 6G was applied onto the photocatalyst surface, then spread over the area of 2 cm^2 and left for drying; the resultant surface concentration of the probing dye was of *ca.* 2×10^{-8} mol/cm^2. The photodegradation of probing dye was followed by measuring a diffuse reflectance, R, at 530 nm that corresponds to the absorption of the dye in the adsorbed state. Using the Kubelka–Munk function [21], the value proportional to the surface dye concentration, Γ , was calculated as follows: $\Gamma \sim (1\text{-}R)^2/2R$.

The ROS production at air-photocatalyst interface was studied by measuring chemiluminescence according to the procedure described in detail elsewhere [6,8].

The glass plates coated with TiO_2 and $TiO_2:MoO_3$ films were illuminated in empty quartz cell with UV light for 30 min. Immediately after illumination the cell was placed into homemade setup permitting the measurement of the chemiluminescence as a function of time. During the course of chemiluminescence measurements the cell was filled with aqueous solution (pH 9) containing 0.4 g/l of luminol and 10^{-4} M $FeSO_4$. The same solution but without $FeSO_4$ additive was used to distinguish peroxo and superoxide species.

Ultraviolet illumination was carried out using high-pressure hydrogen lamp Philips HPK 125 W. The intensity of the incident light was ~ 10 mW/cm^2. The ESR investigations of Mo(V) photoproduction were carried out with the use of powdered samples of $TiO_2:MoO_3$ composite and $SiO_2:MoO_3$ composite (*i.e.*, MoO_3 microcrystals dispersed in the inert silica matrix). The ESR spectra were recorded with a Bruker EMX-8 (X-band) spectrometer at room temperature. The electrochemical measurements were performed with the use of Autolab PGSTAT 204. All the potentials are given against Ag/AgCl, Cl$^-$(sat.) reference electrode. The electrochemical properties of MoO_3 dispersions were investigated by cyclic voltammetry with the use of the carbon paste electrode prepared by mixing 60 mg of carbon powder, 100 mg of molybdenum oxide, and 0.05 ml of dibutylphtalate. For the photoelectrochemical experiments TiO_2 and $TiO_2:MoO_3$ films were deposited onto ITO conducting glass.

3. Results and Discussion

The MoO_3 particles used for $TiO_2:MoO_3$ composite preparation possesses principally different morphology as evidenced by SEM images given in Fig. 1. However, the polycondensation synthetic technique in all cases yields oxide phases of very similar composition: the XRD analysis (presented in the Supplementary Material) evidences that the resultant oxide particles consist of *h*-MoO_3 with the admixture of monoclinic $MoO_3 \bullet 2H_2O$ (the concentration of dihydrate does not exceed

3% in the case of nanoprisms and reaches the maximum value of *ca.* 27% in the case of needle-like crystallites – see the Supplementary Material).

The photodegradation curves for Rhodamine 6G deposited onto the surface of TiO_2 and $TiO_2:MoO_3$ coatings shown in Fig. 2 evidence that photocatalytic degradation of probing dye occurs much more efficiently as compared to the direct photolysis on the surface of a glazed tile free of the photocatalyst. The photocatalytic behavior of $TiO_2:MoO_3$ composite coating appears to be dependent on the type of MoO_3 particles used for composite preparation: while the composite films prepared with the use of nano- and microprisms exhibit the enhanced activity towards probing dye photooxidation under UV irradiation (the rate constant of this process in the case of composite film derived with the use of microprisms is 1.3 times larger than the rate constant of dye photooxidation at bare titania), the composite prepared with the use of spherical MoO_3 nanoparticles and needle-like crystals are less active in comparison with TiO_2. The rate of dye photodegradation is also dependent on the photocatalyst composition; thus, in the case of $TiO_2:MoO_3$ film prepared with the use of MoO_3 microcroprisms, dye photodegradation rate reaches its maximum at MoO_3 loading of *ca.* 15 mol.% and appears to be about 2 times greater than that attained at TiO_2, while at the MoO_3 content larger than 20 mol.% the photooxidation efficiency appears to be lower than that demonstrated by bare titania.

The photoelectrochemical measurements (Fig. 3) evidence that $TiO_2:MoO_3$ coatings containing 15 mol.% of MoO_3 generate photocurrent with the efficiency which is *ca.* 50% greater than that provided by bare TiO_2 pointing to higher yield of photoholes and lower level of recombination losses in the case of composite coating. The latter fact can be attributed to the efficient separation of photoproduced charge carriers at TiO_2/MoO_3 inner heterojunctions that is facilitated by considerable difference in the flat-band potentials of TiO_2 and MoO_3 (this difference estimated from the photocurrent onset potentials for TiO_2 and MoO_3 films used in this work amounts 0.55 V). This improvement in the charge separation ability can be

considered as the key factor responsible for the enhanced photocatalytic activity demonstrated by TiO_2:MoO_3 composite films. However, since the bare MoO_3 demonstrates much lower intrinsic photoactivity as compared to TiO_2, the enhancement of dye photooxidation ability is observed at relatively low MoO_3 loading when one goes from TiO_2 to TiO_2:MoO_3 (Fig. 2b). The trapping of non-equilibrium electrons in the MoO_3 phase results in its reduction as evidenced by ESR measurements (Fig. 4), the latter process being accompanied with formation of hydrogen molybdenum bronzes H_xMoO_3 of variable composition [22]; the MoO_3 reduction leads to the accumulation of the photoinduced negative charge. Although the contribution of superoxide ions into the oxidation activity of TiO_2:MoO_3 composite is marginal (the photoelectrons are mostly involved in the reduction of MoO_3), the low level of recombination losses exhibited by composite photocatalyst results in high yield of hydroxyl radicals that enhances the overall photooxidation activity of the composite films. The photoinduced reduction of MoO_3 in TiO_2:MoO_3 composite occurs much more efficiently than in the case of direct photoreduction of MoO_3 in SiO_2:MoO_3 composite as evident by rapid growing of concentration of paramagnetic Mo(V) centers as shown by ESR measurements (Fig.4a). Under dark conditions the photoinduced Mo(V) centers exhibit slow degradation (Fig. 4b) due to gradual oxidation with air oxygen.

The water contact measurements demonstrate that the composite film exhibits lower intrinsic hydrophylicity as compared to TiO_2 film (Table 1): thus, the contact angle amounts 50°, while in the case of bare TiO_2 it does not exceed 14°. Due to the small fractional area of MoO_3 at the heterogeneous binary surface of composite film the observed decrease in the hydrophylicity in the case of TiO_2:MoO_3 composite can be attributed to the changes in the geometric structure of the photocatalyst surface [8]. It is seen from AFM images given in Fig. 5 that the size of building blocks forming the surface of TiO_2 film exhibits a considerable decrease when going to the surface of TiO_2:MoO_3 composite film; correspondingly, the root mean square

roughness evaluated from AFM 5 μm $\times$ 5 μm plots decreases by 43% (from 158 nm to 110 nm) as one goes from TiO_2 to TiO_2:MoO_3. Note that in the case of photocatalytic coatings under consideration the geometrical factor should determine to large extend the specific contact angle values for their intrinsically hydrophilic surfaces since the size of morphological elements at these surfaces far exceeds lower size limit of chemically distinct patches capable to affect the contact angle which was roughly estimated to be lower than 0.1 μm [23]. The observed decrease of the roughness in the case of composite films can be attributed to the well-known fact of a mutual protective action of composite-forming oxide components against their crystallization that hampers rearrangements in the composite film during an annealing [8,24].

Under actinic illumination, the water contact angle exhibits a decrease in the case of TiO_2 and TiO_2:MoO_3 films, reaching $\sim$ 2° for TiO_2 and 31° for TiO_2:MoO_3 composite. Although the surface of composite film does not exhibit superhydrophylic properties, relatively low contact angle value inherent in it should facilitate water adsorption from humid air that creates favorable conditions both for generation of hydroxyl radicals and for stabilization of photoproduced Mo(V) states in the molybdenum oxide *via* formation of hydrogen molybdenum bronzes.

Notwithstanding to the fact that illumination results in the accumulation of reductive energy, the surface of pre-exposed TiO_2:MoO_3 composite film demonstrates high oxidation activity. It is seen from Fig. 6a that degradation of probing dye occurs over prolonged period after termination of illumination in contrast to bare TiO_2 film showing very rapid decay of its oxidation activity in the dark since the lifetime of superoxide ions (the most long-lived ROS) photoproduced at the titania surface does not exceed 50 s [6]. High oxidation activity inherent in TiO_2:MoO_3 composite films retaining a long time after exposure can be attributed to the fact that one-electron oxidation of photogenerated hydrogen molybdenum bronzes is accompanied with generation of highly reactive species capable to oxidize the probing dye. In principle,

both superoxide and peroxo species are expected to be produced in this reaction. However, it is seen from Fig.7 that the chemiluminescent signal resulting from interaction of luminol with these species is detected only in the presence of Fe^{2+} evidencing that the oxidation of H_xMoO_3 by molecular oxygen leads to the formation of just the peroxo species. In the presence of Fe(II) these species yield hydroxyl radicals *via* Fenton reaction and these radicals interact with luminol emitting chemiluminescence. On the other hand, the absence of chemiluminescent signal in contact with the Fe^{2+}-free solution of luminol allows conclusion that superoxide production at the surface of $TiO_2:MoO_3$ composite photocatalyst is suppressed and photoelectrons generated in TiO_2 and MoO_3 are predominantly trapped in the MoO_3 particles. From this point of view the $TiO_2:MoO_3$ composite differ radically from bare TiO_2 capable to generate considerable amounts of O_2^- species responsible to the large extent for its oxidation ability [6,8]. The chemiluminescence measurements also provide evidence that peroxo species are detectible at the $TiO_2:MoO_3$ composite surface for a long time after UV exposure (Fig. 7).

It is seen from Fig. 6a that the oxidation activity of the pre-exposed $TiO_2:MoO_3$ composite photocatalyst is dependent on the morphology of the MoO_3 phase used for composite synthesis: thus, the composite photocatalyst obtained with the use of MoO_3 spherical nanoparticles looses the ability to oxidize probing dye in an hour, while composite obtained with the use of MoO_3 prismatic crystals of submicron size (nanoprisms) retains the pronounced oxidation ability for a long time. On the other hand, these fine MoO_3 crystals resulting from the splitting of large MoO_3 microprisms [19] show the most pronounced ability to accumulate negative charge as evidenced by cyclic voltammograms given in Fig. 8. The highly effective reduction behavior demonstrated by these nanocrystals [25] can be attributed to high surface-to-volume ratio inherent to them and their perfect structure that creates favorable conditions for proton transport along the lamellae. By contrast, the MoO_3 microprisms and needle-like microcrystals with a large admixture of $MoO_3 \cdot 2H_2O$

seem to be highly defective and, as the result, show much lower activity in electrochemical experiments as compared to MoO_3 nanoprisms (Fig. 8) notwithstanding to the fact that dihydrate phase also possesses a layered structure. Nanoparticles of spherical shape exhibit much worse access for protons to the interlaminar space and much less ability to the reduction (Fig. 8).

The progressive oxidation of the hydrogen molybdenum bronzes by atmospheric oxygen occurs slowly being controlled by proton transport in the solid phase and the oxidation activity of TiO_2:MoO_3 composite retains for the long time: it is seen from Fig. 6b that for composite films prepared with the use of MoO_3 microprisms the rate of probing dye oxidation drops to zero in an hour, while for composite prepared with the use of MoO_3 prismatic crystals of submicron size the zero oxidation rate is attained in 4 hours.

4. Conclusions

The present study shows that nanocomposite photocatalyst in which TiO_2 is combined with h-MoO_3 exhibits excellent photoenergy storage abilities resulted from the accumulation of the photoinduced charge in the form of hydrogen molybdenum bronzes. Due to layered structure inherent in h-MoO_3, the process of its reduction controlled by proton transport extends over the bulk MoO_3 crystals of sub-micron size. Generation of peroxide species during the course of oxidation of hydrogen molybdenum bronzes with molecular oxygen imparts high oxidation activity to the pre-exposed TiO_2:MoO_3 composite coatings, this activity retaining for a long time (up to 4 h after the moment when the illumination was stopped). The efficient trapping of photoelectrons in MoO_3 also enhances the oxidation activity of TiO_2:MoO_3 composite films under actinic illumination. This makes nanoengineered TiO_2:MoO_3composite a candidate for self-sterilizing coatings exhibiting oxidation activity both under illumination and under dark conditions.

References

[1] D. Bahnemann, Photocatalytic water treatment: solar energy applications, Solar Energy 77 (2004) 445–459.

[2] A. Fujishima, T.N. Rao, D.A. Truk, Titanium dioxide photocatalysis, J. Photochem. Photobiol. C: Photochem. Rev. 1 (2000) 1–21.

[3] A.G. Agrios, P. Pichat, State of the art and perspectives on materials and applications of photocatalysis over TiO_2, J. Appl. Electrochem. 35 (2005) 655–663.

[4] D.G. Shchukin, D.V. Sviridov, Photocatalytic processes in spatially confined micro- and nanoreactors, J. Photochem. Photobiol. C: Photochem. Rev. 7 (2006) 23–26.

[5] K. Ishibashi, A. Fujishima, T. Watanabe, K. Hashimoto, Quantum yields of active oxidative species formed on TiO_2 photocatalyst, J. Photochem. Photobiol. A: Chemistry 134 (2000) 139–142.

[6] K. Ishibashi, A. Fujishima, T. Watanabe, K. Hashimoto, Generation and deactivation processes of superoxide formed on TiO_2 film illuminated byvery weak UV light in air or water, J. Phys. Chem. B 104 (2000) 4934-4938.

[7] M.R. Hoffmann, S.T. Martin, W. Choi, D.W. Bahnemann, Environmental applications of semiconductor photocatalysis, Chem. Rev. 95 (1995) 69–96.

[8] E.V. Skorb, Elena A. Ustinovich, A. I. Kulak, D. V. Sviridov, Photocatalytic activity of TiO_2:In_2O_3 nanocomposite films towards the degradation of arylmethane and azo dyes, J. Photochem. Photobiol. A: Chemistry. 193 (2008) 97–102.

[9] Z. Huang, P.-C. Maness, D.M. Blake, E.J. Wolfrum, S.L. Smolinski, W.A. Jacoby, Bactericidal mode of titanium dioxide photocatalysis, J. Photochem. Photobiol. A: Chem. 130 (2000) 163–170.

[10] K. Sunada, T. Watanabe, K. Hashimoto, Studies on photokilling of bacteria on TiO2 thin film, J. Photochem. Photobiol. A: Chem. 156 (2003) 227–233.

[11] E.V. Skorb, L.I. Antonouskaya, N.A. Belyasova, D.G. Shchukin, H. Möhwald, D.V. Sviridov, Antibacterial activity of thin-film photocatalysts based on metal-

modified TiO_2 and TiO_2:In_2O_3 nanocomposite, Appl. Catal. B: Environmental 84 (2008) 94–99.

[12] T. Tatsuma, S. Saitoh, P. Ngaotrakanwiwat, Y. Ohko, A. Fujishima, Energy storage of TiO_2-WO_3 photocatalysis systems in the gas phase, Langmuir 18 (2002) 7777-7779.

[13] T.Tatsuma, S. Takeda, S. Saitoh, Y. Ohko, A. Fujishima, Bactericidal effect of an energy storage TiO_2–WO_3 photocatalyst in dark, Electrochem. Comm. 5 (2003) 793–796.

[14] Y. Takahashi, T. Tatsuma, Visible light-induced photocatalysts with reductive energy storage abilities, Electrochem. Comm. 10 (2008) 1404–1407.

[15] D. Liu, W. Zi, S. D. Sajjad, C. Hsu, Y. Shen, M. Wei, F. Liu, Reversible electron storage in an all-vanadium photoelectrochemical storage cell: Synergy between vanadium redox and hybrid photocatalyst, ACS Catal. 5(2015) 2632–2639.

[16] Y. Takahashi, P. Ngaotrakanwiwat, T. Tatsuma, Energy storage TiO_2–MoO_3 photocatalysts, Electrochim. Acta 49 (2004) 2025–2029.

[17] P. Ngaotrakanwiwat, S. Saitoh, Y. Ohko, T. Tatsuma A. Fujishima, TiO_2 - phosphotungstic acid photocatalysis systems with an energy storage ability, J. Electrochem. Soc. 150 (2003) A1405-A1407.

[18] F. Yang, Y. Takahashi, N. Sakai, T. Tatsuma, Visible light driven photocatalysts with oxidative energy storage abilities, J. Mater. Chem. 21(2011) 2288-2293.

[19] T.V. Sviridova, L.I. Stepanova, D.V Sviridov, Nano- and microcrystals of molybdenum trioxide and metal-matrix composites on their basis, in: M. Ortiz, T. Herrera (Eds.), Molybdenum: Characteristics, Production and Applications, Nova Sci. Publishers, New York, 2012, pp. 147-179.

[20] H. Tada, M. Tanaka, Dependence of TiO_2 photocatalytic activity upon its film thickness, Langmuir 13 (1997) 360-364.

[21] W. Wedland, H. Hecht, Reflectance Spectroscopy, Intersci. Publ., New York, 1966.

[22] O. Zelaya-Angel, C. Menezes, F. Sánchez-Sinencio, G.F.L. Ferreira, Electron diffusion and electrochromism in MoO_3 amorphous films, J. Appl. Phys. 51(1980) 6022-6026.

[23] A.W. Neumann, Contact angles and their temperature dependence: thermodynamic status, measurement, interpretation and application, Adv. Colloid Interf. Sci. 4 (1974) 105.

[24] S. K. Poznyak, D. V. Talapin, A. I. Kulak, Structural, optical, and photoelectrochemical properties of nanocrystalline TiO_2-In_2O_3 composite solids and films prepared by sol-gel method, J. Phys. Chem. B 105 (2001) 4816-4823.

[25] T.V. Sviridova, L.I. Stepanova, D.V Sviridov, Electrochemical synthesis of Ni-MoO_3 composite films: redox-mediated mechanism of electrochemical growth of metal-matrix composite, J. Solid-State Electrochem. 16 (2012) 3799-3803.
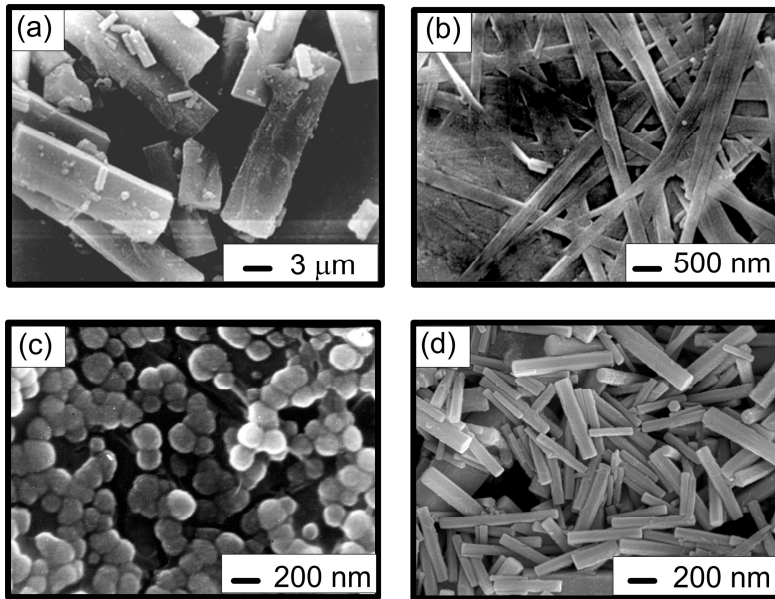
Figure 1. A typical SEM image showing the general morphology of MoO_3 particles used for TiO_2:MoO_3 composite synthesis: (a) microprisms, (b) needle-like microcrystals, (c) spherical nanoparticles, (d) nanoprisms.
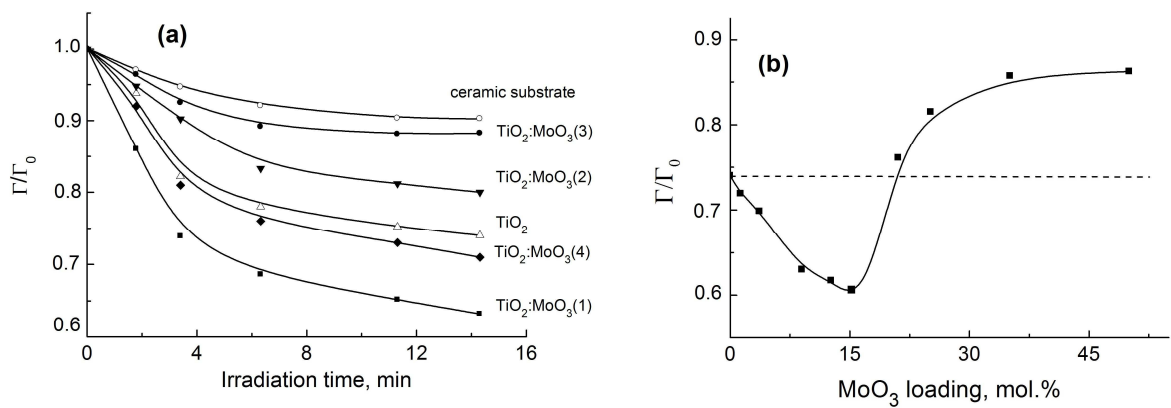
Figure 2. (a) Photodegragation kinetics of Rhodamine 6G on TiO_2 and TiO_2:MoO_3 thin-film photocatalysts as well as on the glazed tile used as the substrate. Composites were prepared using different MoO_3 phases: (1) microprisms, (2) needle-like microcrystals, (3) spherical nanoparticles, (4) nanoprisms. MoO_3 loading was of 15 mol.%. Γ_0 and Γ are the initial concentration of a probing dye and after irradiation.

Ambient humidity: 45%. (b) Dependence of the relative drop of dye concentration after 15 min irradiation on the MoO_3 loading for $TiO_2:MoO_3$ (1) composite. The dashed line shows a drop of dye concentration fat bare TiO_2.
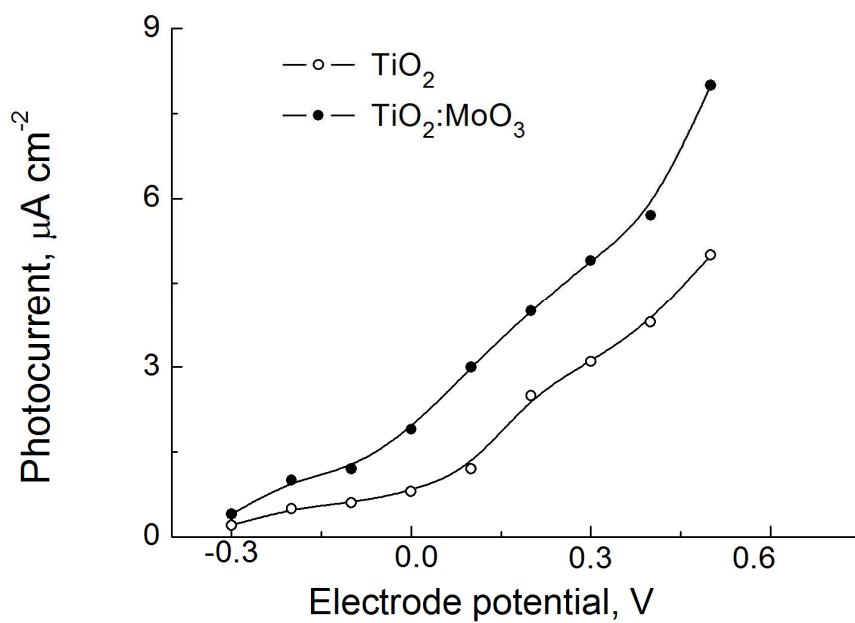
Figure 3. Photocurrent versus potential curves for TiO_2 and $TiO_2:MoO_3$ films. For composite preparation MoO_3 nanoprisms were used, the MoO_3 loading was of 15 mol.% Electrolyte: 0.25 M Na_2SO_4 + 0.1M CH_3COONa.
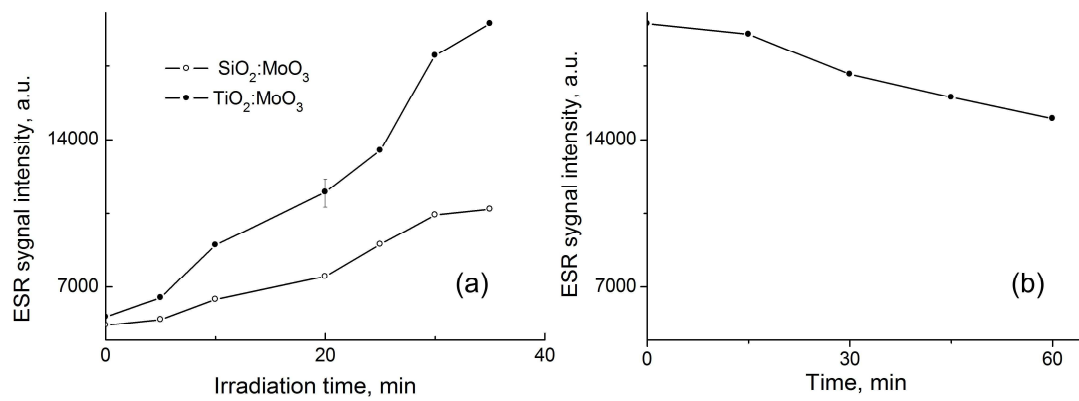
Figure 4. (a) The ESR signal intensity as a function of UV irradiation time for SiO_2:MoO_3 and TiO_2:MoO_3. For composite preparation MoO_3 nanoprisms were used. The MoO_3 loading in composites was of 15 mol.%. (b) The ESR signal intensity decay for pre-exposed TiO_2:MoO_3 composite.
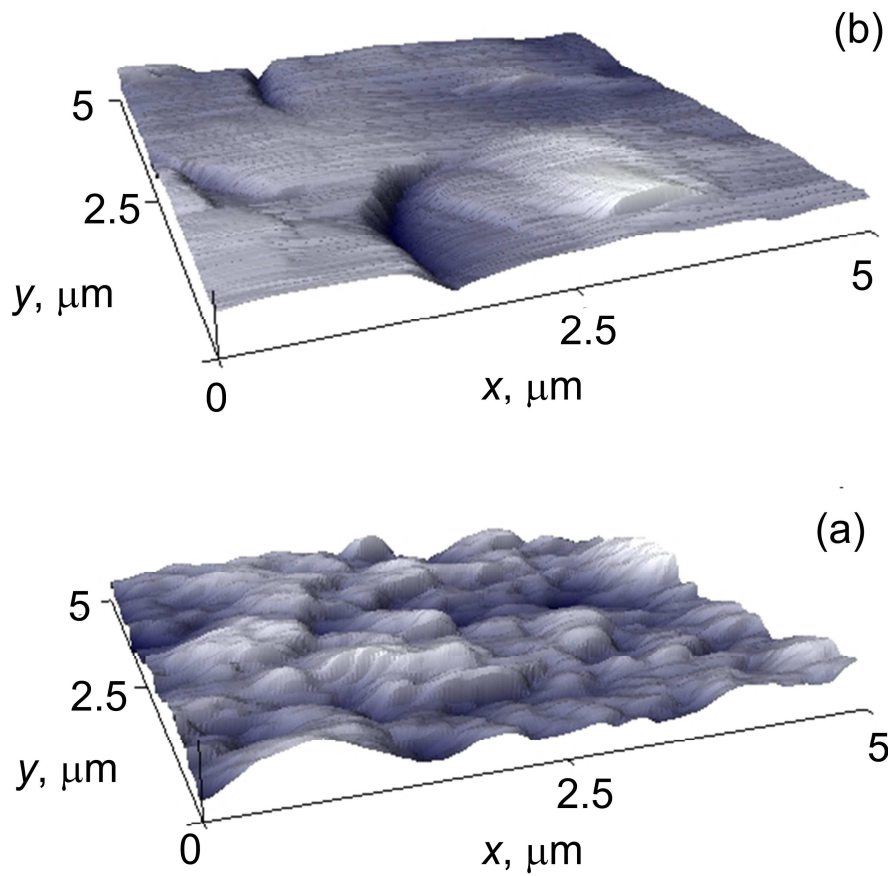
Figure 5. AFM surface plots for (a) TiO_2 and (b) TiO_2:MoO_3 films. For composite preparation MoO_3 nanoprisms were used. MoO_3 loading was of 15 mol.%.
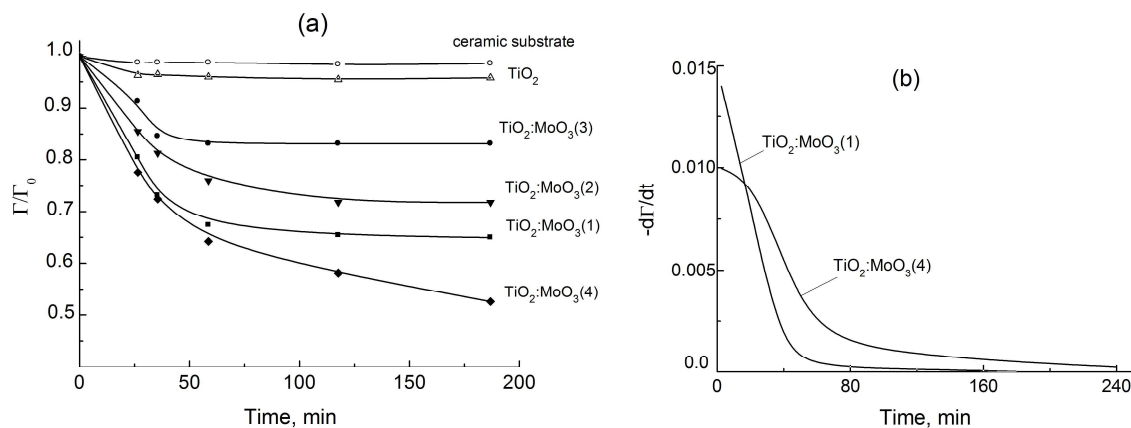
Figure 6. (a) Degradation kinetics of Rhodamine 6G on the pre-exposed TiO_2 and TiO_2:MoO_3 photocatalysts under dark conditions. Composites were prepared with the use of: (1) microprisms, (2) needle-like microcrystals, (3) spherical nanoparticles, (4) nanoprisms. MoO_3 loading was of 15 mol.%. Before measurements, samples were exposed to UV light for 30 min. (b) Time dependence of the dye degradation rate.
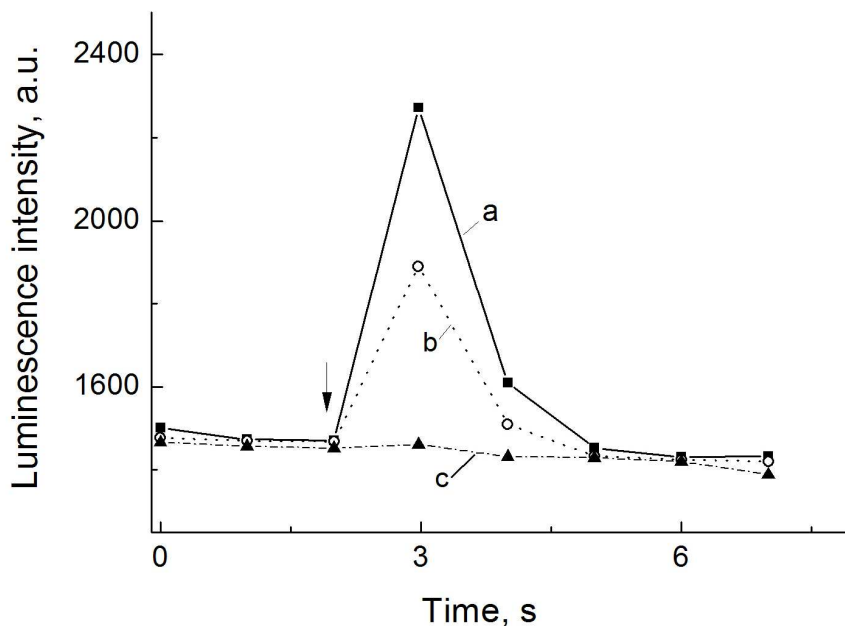

Figure 7. Time profiles of the chemiluminescence intensity for TiO_2:MoO_3 composite film exposed to UV light for 30 min. The arrow indicates the moment corresponding to the insertion of: (curves *a*, *b*) luminol $+$ Fe^{2+} solution; (curve *c*)

luminol solution. Curve *b* recorded for pre-exposed $TiO_2:MoO_3$ composite film left in dark for 40 min. The $TiO_2:MoO_3$ composite was synthesized using MoO_3 nanoprisms, MoO_3 loading was of 15 mol. %.
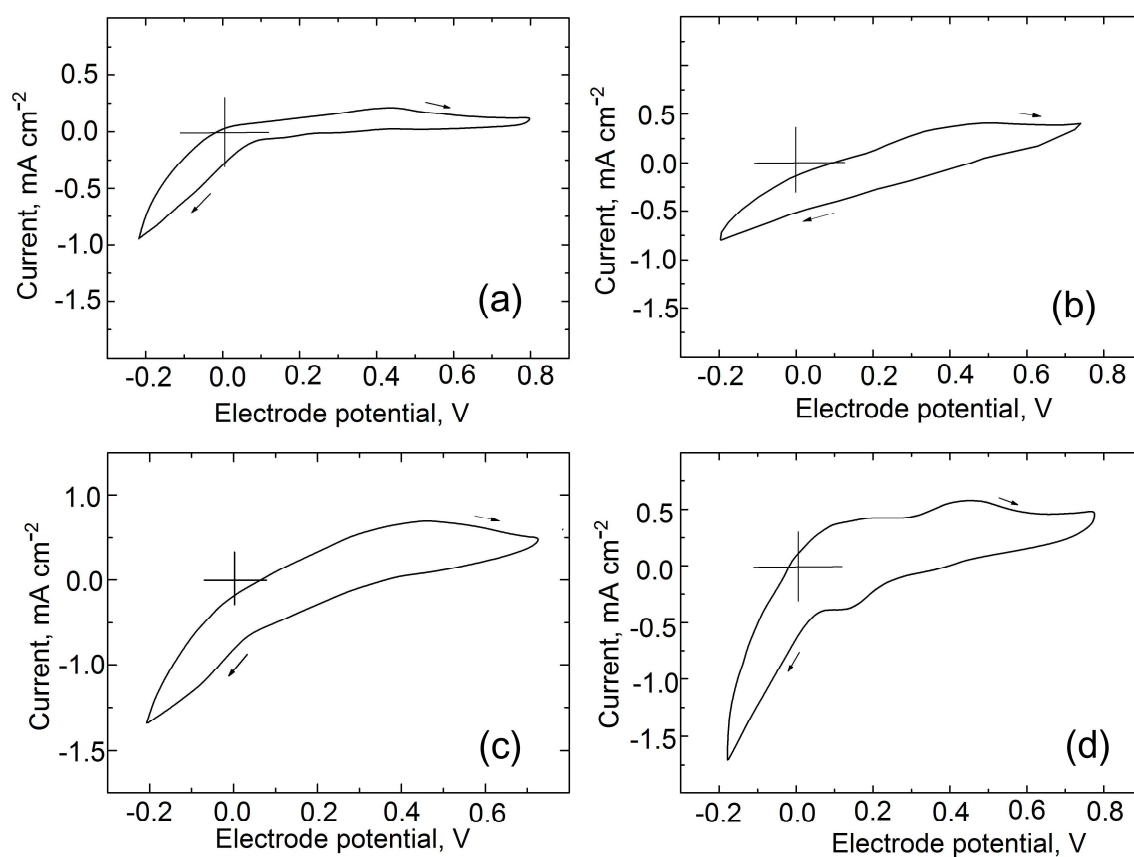

Figure 8 Cyclic voltamperogramms for MoO_3-loaded carbon paste electrode. MoO_3 phase: (a) microprisms, (b) needle-like microcrystals, (c) spherical nanoparticles, (d) nanoprisms. Electrolyte: deaerated 0.25 M Na_2SO_4, pH 4.5. The potential scan rate is 0.1 V/s.

Table 1

The water contact angle for bare TiO_2 and $TiO_2:MoO_3$ composites*

Photocatalytic coating	TiO_2	$TiO_2:MoO_3(1)$	$TiO_2:MoO_3(2)$	$TiO_2:MoO_3(3)$	$TiO_2:MoO_3(4)$
In the dark conditions	14	50	53	51	43
After UV illumination for 30 min	2	31	40	33	25

*) the notation of composites prepared with the use of different MoO_3 particles is similar to that in Fig.2

Supplementary Material

to the paper *Nanoengineered Thin-film TiO$_2$/h-MoO$_3$ Photocatalysts Capable to Accumulate Photoinduced Charge*

The X-ray diffraction analysis of MoO$_3$ particles of different morphology (microprisms, needle-like microcrystals, nanospherulites, nanoprisms) prepared *via* polycondensation of molybdic acid in aqueous medium has evidenced that the resultant oxide products consist of hexagonal molybdenum oxide and monoclinic molybdenum oxide dihydrate MoO$_3$ (Tables S1-S4). The MoO$_3$·2H$_2$O content was estimated from the thermogravimetric measurements (Table S5).

Table S1

Powder X-ray diffraction data for MoO$_3$ microprisms

Experimental data		Data from Refs. 1,2			
d, Å	*I/I$_{100}$*,%	Compound	*d*, Å	*I/I$_{100}$*. %	*hkl*
9.10	80	MoO$_3$	9.120	80	100
6.850	100	MoO$_3$·2H$_2$O	6.900	100	020
5.285	15	MoO$_3$	5.290	10	110
4.558	70	MoO$_3$	4.560	20	200
3.767	25	MoO$_3$·2H$_2$O	3.770	30	400
3.450	100	MoO$_3$	3.450	100	210
3.038	10	MoO$_3$	3.040	40	300
2.881	1	MoO$_3$	2.880	5	204
2.629	20	MoO$_3$	2.630	10	220
2.529	27	MoO$_3$	2.530	30	310
2.301	95	MoO$_3$·2H$_2$O	2.305	12	-514
2.145	2	MoO$_3$	2.147	5	224
2.093	25	MoO$_3$	2.097	10	320
1.990	45	MoO$_3$	1.993	20	410
1.945	5	MoO$_3$	1.947	15	404
1.855	1	MoO$_3$	1.860	15	008
1.821	10	MoO$_3$	1.824	10	500

Powder X-ray diffraction data for MoO_3 needle-like microcrystals

Experimental data		Data from Refs. 1,2			
d, Å	I/I_{100},%	Compound	d, Å	I/I_{100}. %	*hkl*
9.61	48	MoO_3	9.690	80	100
6.850	100	$MoO_3 \cdot 2H_2O$	6.900	100	020
5.288	9	MoO_3	5.290	10	110
4.554	33	MoO_3	4.560	20	200
3.763	12	$MoO_3 \cdot 2H_2O$	3.770	30	400
3.447	100	MoO_3	3.450	100	210
3.236	75	$MoO_3 \cdot 2H_2O$	3.240	45	024
3.036	3	MoO_3	3.040	40	300
2.639	6	MoO_3	2.630	10	220
2.530	10	MoO_3	2.530	30	310
2.297	75	$MoO_3 \cdot 2H_2O$	2.305	12	-514
2.101	9	MoO_3	2.097	10	320
1.997	15	MoO_3	1.997	20	410
1.946	4	MoO_3	1.947	15	404
1.822	6	$MoO_3 \cdot 2H_2O$	1.823	6	-108

Powder X-ray diffraction data for MoO_3 nanospherulites

Experimental data		Data from Refs. 1,2			
d, Å	I/I_{100},%	Compound	d, Å	I/I_{100}. %	hkl
9.11	50	MoO_3	9.120	80	100
6.870	100	$MoO_3 \cdot 2H_2O$	6.900	100	020
5.305	7	MoO_3	5.290	10	110
4.550	30	MoO_3	4.560	20	200
3.605	1	$MoO_3 \cdot 2H_2O$	3.770	30	400
3.448	100	MoO_3	3.450	100	210
3.035	20	MoO_3	3.040	40	300
2.876	2	MoO_3	2.880	5	204
2.630	8	MoO_3	2.630	10	220
2.526	20	MoO_3	2.530	30	310
2.310	95	$MoO_3 \cdot 2H_2O$	2.305	12	-514
2.145	2	MoO_3	2.147	5	224
2.088	10	MoO_3	2.097	10	320
1.990	20	MoO_3	1.993	20	410
1.945	7	MoO_3	1.947	15	404
1.864	5	MoO_3	1.860	15	008
1.820	3	MoO_3	1.824	10	500

Powder X-ray diffraction data for MoO_3 nanoprisms

Experimental data		Data from Refs. 1,2			
d, Å	I/I_{100},%	Compound	d, Å	I/I_{100}. %	hkl
9.10	40	MoO_3	9.120	80	100
6.950	100	$MoO_3 \cdot 2H_2O$	6.900	100	020
5.285	7	MoO_3	5.290	10	110
4.620	33	MoO_3	4.560	20	200
3.425	100	MoO_3	3.450	100	210
3.035	34	MoO_3	3.040	40	300
2.878	15	MoO_3	2.880	5	204
2.625	10	MoO_3	2.630	10	220
2.531	15	MoO_3	2.530	30	310
2.145	2	MoO_3	2.147	5	224
2.098	13	MoO_3	2.097	10	320
1.995	22	MoO_3	1.993	20	410
1.940	5	MoO_3	1.947	15	404
1.862	3	MoO_3	1.860	15	008
1.826	4	MoO_3	1.824	10	500

Content of $MoO_3 \cdot 2H_2O$ in the oxide particles of different morphology used for composite preparation

Oxide particles	Content, %
Microprisms	10
Needle-like microcrystals	27
Nanospherulites	15
Nanoprisms	5

References

1. Powder Diffraction File. Card No 21-569. JCPDS International Centre for Diffraction Data. Swarthmore, 1989.

2. Powder Diffraction File. Card No 16-497. JCPDS International Centre for Diffraction Data. Swarthmore, 1989.